Journal of
Mechanics of
Materials and Structures

INFLUENCE OF SPECIMEN GEOMETRY ON THE PORTEVIN–LE CHÂTELIER EFFECT DUE TO DYNAMIC STRAIN AGING FOR THE AA5083-H116 ALUMINUM ALLOY

Rodrigo Nogueira de Codes and Ahmed Benallal

Volume 6, No. 7-8 September–October 2011

mathematical sciences publishers

JOURNAL OF MECHANICS OF MATERIALS AND STRUCTURES
Vol. 6, No. 7-8, 2011

INFLUENCE OF SPECIMEN GEOMETRY ON THE PORTEVIN–LE CHÂTELIER EFFECT DUE TO DYNAMIC STRAIN AGING FOR THE AA5083-H116 ALUMINUM ALLOY

RODRIGO NOGUEIRA DE CODES AND AHMED BENALLAL

Digital image correlation and digital infrared thermography are employed to capture and characterize the spatiotemporal aspects of the Portevin–Le Châtelier phenomenon due to dynamic strain aging in various types of specimens. Deformation bands are visualized and the effects of the specimen shape on the morphology of the bands are underlined. Further, while the deformation bands are usually seen to propagate along the whole gauge length of smooth specimens, they are observed here to be generally trapped around stress concentrators.

1. Introduction

The mechanical behavior of AA5083-H116 aluminum alloy exhibits irregular plastic flow in a given range of strain rates and temperatures [Clausen et al. 2004; Benallal et al. 2008a; 2008b]. In a uniaxial tension test for instance, this irregular flow results in inhomogeneous deformation with different types of localization bands. These bands can be static, hopping, or even propagating along the specimen when the strain rate is increased or the temperature decreased. It is also observed in the presence of this irregular flow that the material often fails by a shear localization mode prior to any significant diffuse necking.

It is widely accepted that this irregular flow is the consequence of negative strain-rate sensitivity due to dynamic strain aging, that is, the solute-dislocation interaction at the microscopic level, although a firm mechanism for the diffusion process is not established for aluminum alloys. Indeed, while Cottrell's theory on immobilization of dislocations by solute atmospheres is agreed to be involved in a way or another, various mechanisms for the diffusion and segregation of solute atoms to dislocations have been proposed and criticized [Nabarro 1948; Cottrell 1953a; 1953b; Sleeswyk 1958; Mulford and Kocks 1979; van den Beukel 1980; McCormick 1988]. The debate over the mechanisms is still going on in recent proposals [Picu 2004; Curtin et al. 2006].

The results of dynamic strain aging are higher flow stress and greater strain hardening rates at lower strain rates than at higher ones. The phenomenon also referred to as the Portevin–Le Châtelier (PLC) effect is observed in a number of dilute solid solutions (with BCC and FCC, but also HCP, crystal structures). A number of reviews on the phenomenon are available in the literature; see [Kubin and Estrin 1985; Robinson and Shaw 1994; Neuhäuser et al. 2004; Rizzi and Hähner 2004].

The PLC effect is a technologically important problem because it adversely affects the formability of the material. Inhomogeneous plastic straining increases geometrical perturbations in a component and thus reduces the strain to necking. Further, the propagating deformation bands give rise to undesired markings on the surface of the shaped material. Hopperstad et al. [2007] showed in a numerical

Keywords: Portevin–Le Châtelier effect, AA5083-H116 aluminum alloy, specimen geometry, dynamic strain aging.

study, taking into account dynamic strain aging and negative strain-rate sensitivity through the model of [McCormick 1988], that PLC effects can lead to significant reduction in the strain to necking both under uniaxial and biaxial tension, rendering this type of information vital in metal forming, for instance.

An extensive experimental program has been designed by the authors and their coworkers to understand the features of the PLC effect on AA5083-H116 aluminum alloy, where this effect is pronounced and almost unstudied in the literature. Thus the effects of strain rate and temperature on the appearance of this phenomenon were studied in [Clausen et al. 2004; Benallal et al. 2008a; 2008b]. Various tension tests were carried out on smooth specimens in order to exhibit the PLC domain and further characterize the various observed deformation bands. Strain rates ranging from $10^{-7}\,\mathrm{s}^{-1}$ to $103\,\mathrm{s}^{-1}$ and temperatures going from -75° C to 500° C were considered on flat and round smooth specimens.

The objective of this paper is to extend the former observations by analyzing the effects of specimen geometry and specimen dimensions on the features of the PLC effect. Various types of specimens are thus considered and subjected to tension loadings. Digital image correlation (DIC) and digital infrared thermography (DIT) are used to capture and characterize the spatiotemporal aspects of the PLC effect. Inhomogeneous deformation with different localization bands is observed on the different specimens. Also, deformation bands are visualized showing their formation, evolution, and propagation. This visualization also allows the morphology of the bands to be studied and their characteristics to be measured.

2. Material and experimental program

The material studied in this investigation is the aluminum alloy AA5083-H116. The main alloying elements are magnesium with 4.4 weight percent, manganese with 0.7 weight percent, and chromium with 0.15 weight percent. AA5083 may also contain minor quantities of elements such as iron, copper, and zinc. It is important to notice that the amount of magnesium is higher than 3 weight percent, which is the maximum to be retained in solid solution at room temperature. This gives a potential instability leading to precipitation along grain boundaries or slip planes. Stress corrosion is thus a likely consequence in corrosive media. Special precautions have to be made during rolling in order to avoid this problem, and the temper H116 was therefore developed.

The AA5xxx series is well suited for rolling, and plates are thus an important product. The traditional use of such plates is in naval structures such as ship hulls and offshore topsides, and the good corrosion resistance of the AA5xxx series gives further reason for these marine applications.

Smooth flat, prismatic, and round specimens are used in this investigation. The smooth round specimens all have a 6 mm diameter, and the prismatic specimens have cross sections $5 \times 5\,\mathrm{mm}^2$ and $5 \times 6\,\mathrm{mm}^2$. Finally, the flat smooth specimens have a width of 15 mm; their thickness were varied with the following values considered: $e = 1, 2, 3, 4, 5, 7,$ and 9 mm. The study is completed with U-notched and V-notched flat specimens. The U-notches have radii of 0.4, 0.8, and 2 mm while the V-notches have angles of 0, 30, 45, and 60°. Note that only one notch was used for the 0° V-notch (cracked specimen). However, the crack was not initiated prior to the loading process.

All the specimens were cut from 5 mm and 10 mm thick rolled plates and their axial directions were aligned with the rolling direction. All the tests considered in the paper were carried out at room temperature in a servohydraulic material-testing machine (MTS model 810) with a 10 kN capacity load cell.

Two different techniques were used to observe and eventually characterize the PLC bands spatially and temporally, namely, DIC and DIT. Zones on the gauge length of all the flat specimens were imaged with a fast CCD camera (model Ultima APX-RS) on one side and with an infrared camera (model JADE 570M) on the other side. Prior to the tests, one side of the specimen was decorated with finely sprayed black and white paints to enhance the image contrast and the other was painted with a fully black paint in order to enhance its emissivity. Only DIT was used for round specimens.

For DIC the recorded digital images had a 256×336 pixel size. Images were recorded at a shutter speed of 125 frames per second.

The principle of DIC is based on the fact that the distribution of grayscale values of a rectangular area in the initial image corresponds to the distribution of grayscale values of the same area in the destination image. A cumulative strain map can be obtained by comparing each current deformation image with the initial image while an incremental strain map can be computed by comparing the image at the current load step with the image recorded just before the current load increment. These maps are computed from the recorded data by the software Correli Hild and Roux [2006].

The image size and acquisition speed for the DIT were 31×65 pixels and 150 frames per second, respectively. The imaged zones for the DIT are sketched in Figure 1 for all the specimens. The imaged zone for the U-notched specimen ($R = 2$ mm) is shown in detail in Figure 1a and zoomed in Figures 1b and 1c, where one can respectively see the locations of different points and three vertical lines ($x = 0.65$, $x = 4.84$, and $x = 9.68$) where some of the experimental results are presented in the next sections.

The tests were carried out at room temperature in a servohydraulic material-testing system (MTS model 810) with a 10 kN load cell (uniaxial tension test).

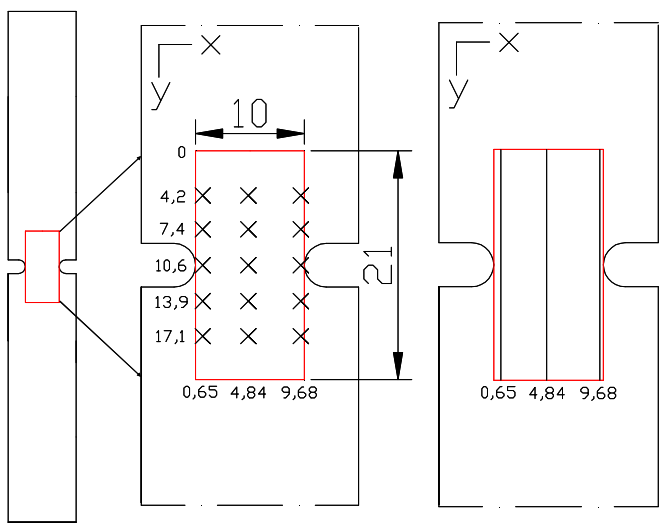

(a) (b) (c)

Figure 1. (a) Flat U-notched specimen with a 2 mm radius notch (T3) used in the investigation showing the imaged zone area for digital infrared thermography (DIT); (b, c) zooms of the imaged area indicating the locations used for presenting some of the experimental results in Section 3.2.

The acquired thermal information was processed in the following manner: at each acquisition time t, the acquired data was a matrix $T(x, y, t)$ representing the chart of temperatures as measured by the infrared camera, with x representing lines (in the transverse direction) and y columns (in the longitudinal direction corresponding to the tension axis), and (x, y) a pixel from the imaged zone in the specimen. To minimize noise in the visualization of the bands, the average temperature change over a time increment δt was considered and expressed mathematically as

$$\Delta T(x, y, t) = \frac{1}{m} \sum_{j=0}^{j=m-1} [T(x, y, t + m\,\delta t) - T(x, y, t + j\,\delta t)], \tag{1}$$

with δt the acquisition shutter speed (in frames per second). The choice of the parameter m depended on the cross-head velocity and acquisition speed during the test. For the tests carried out in this work, $m = 1$ and $m = 10$ were used.

3. Results

3.1. ***Portevin–Le Châtelier effect in uniaxial tension.*** We give in this section, for completeness, some results on experimental observations made during uniaxial tension on smooth specimens. More results and details can be found in [Benallal et al. 2008a; 2008b].

Figure 2 shows the load-displacement curves obtained for different uniaxial tests on different smooth specimens. These curves all show the serrated behavior and it is important to emphasize here the different nature of the serrations observed for each type of specimen.

Figure 3 is a sequence of six images taken at different instants displaying the propagation of a PLC deformation band during a tension test on a round specimen, for a nominal strain-rate of $10^{-1}\,\mathrm{s}^{-1}$. The pictures represent the change $\Delta T(x, y, t)$ given by relation (1) over the imaged zone of the specimen. The temperature change is about 0.5° C. These pictures show the band all over the specimen and depicts

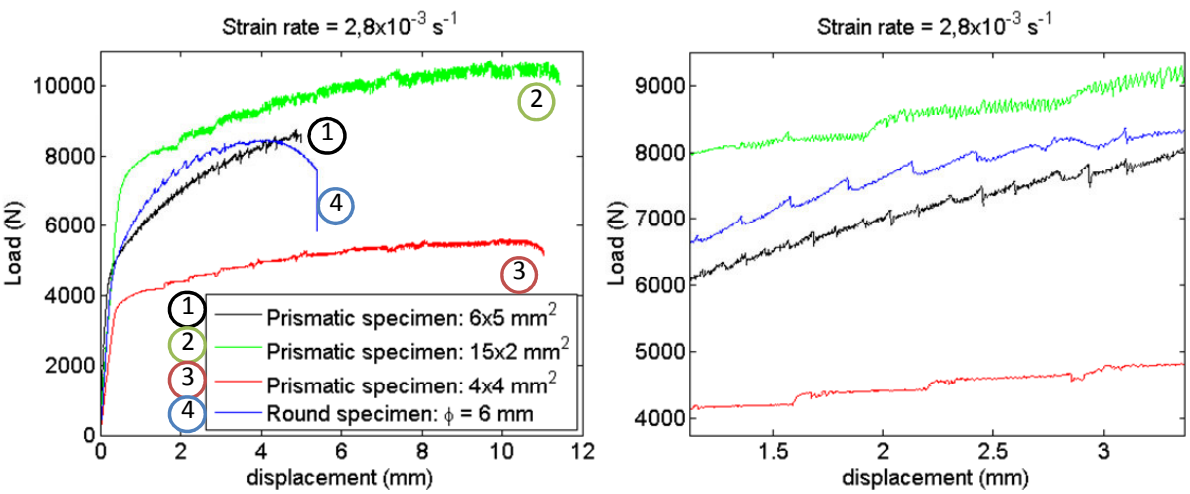

Figure 2. Load-displacement curves for different smooth specimens (left) and zoom of the curves displaying the serrations (right).

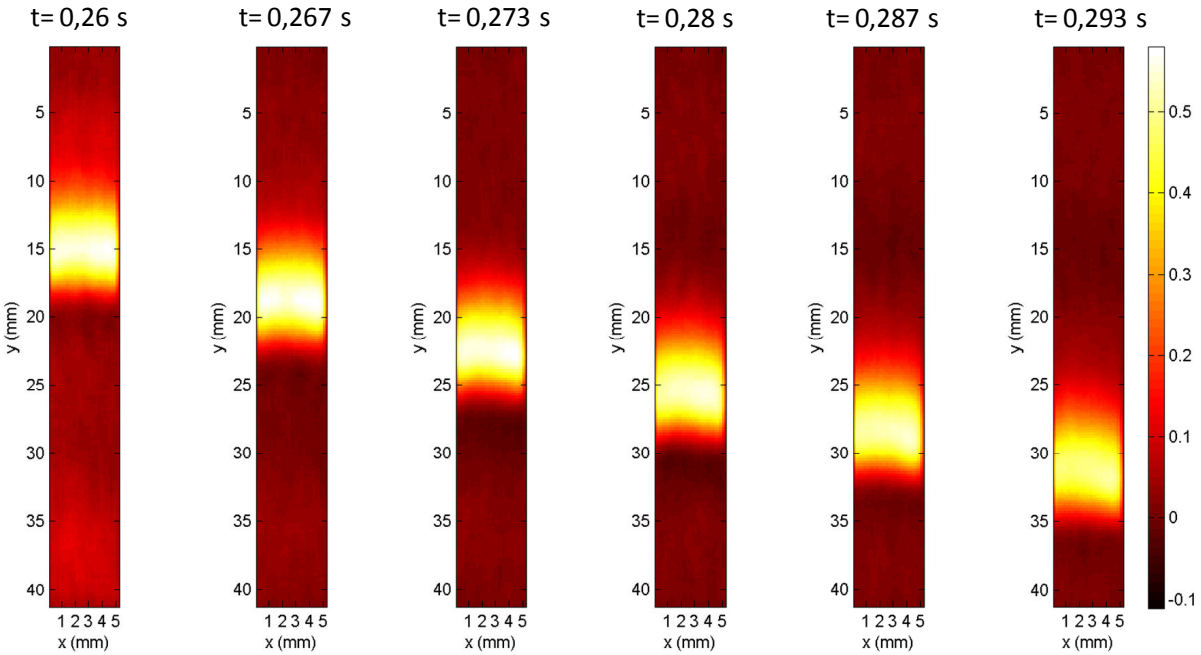

Figure 3. Sequence of six DIT images showing the propagation of a PLC deformation band during a tension test in a round specimen ($\phi = 6\,\text{mm}$) with nominal strain rate $10^{-1}\,\text{s}^{-1}$. The figure displays only the imaged zone of the specimen. The temperature increment ΔT given by (1) is displayed here.

therefore its morphology. The band is inclined at an angle of 52° C with respect to the loading access and has a thickness of about 5 mm.

Figure 4 shows again the PLC deformation bands observed during tension tests on round specimens, during almost the whole tests, for different strain rates ranging from $10^{-5}\,\text{s}^{-1}$ to $10^{-1}\,\text{s}^{-1}$. For clarity, the final phase of the tests, namely rupture of the specimens, has been removed, since the significant temperature rise due to fracture would have masked the deformation bands. Figures 4b–4e display spatiotemporal representations of the temperature change $\Delta T(0, y, t)$ along the vertical centerline of the imaged zone (shown in Figure 4a) as a function of time. For a better interpretation, the load-time curve is also superposed on the figures showing the serrations and associated deformation bands. It is interesting to notice here that at the beginnings of all the tests, the different deformation bands are traveling along the gauge length of the specimens in the same direction, while after a given time or strain, they start traveling back and forth until fracture.

Figure 5 depicts the same spatiotemporal representations for tension tests carried out on different smooth specimen geometries, at the same strain rate of $2.8 \times 10^{-3}\,\text{s}^{-1}$. The deformation band patterns look at a first sight different, but they all consist of type A bands. (A type A band is usually defined as a PLC band that nucleates somewhere in the gauge length of the specimen and continuously propagates along this gauge length.)

Figure 6 shows again the same spatiotemporal representations for tension tests carried out at the same strain-rate of $10^{-2}\,\text{s}^{-1}$ on different smooth flat specimens having the same width but different thicknesses

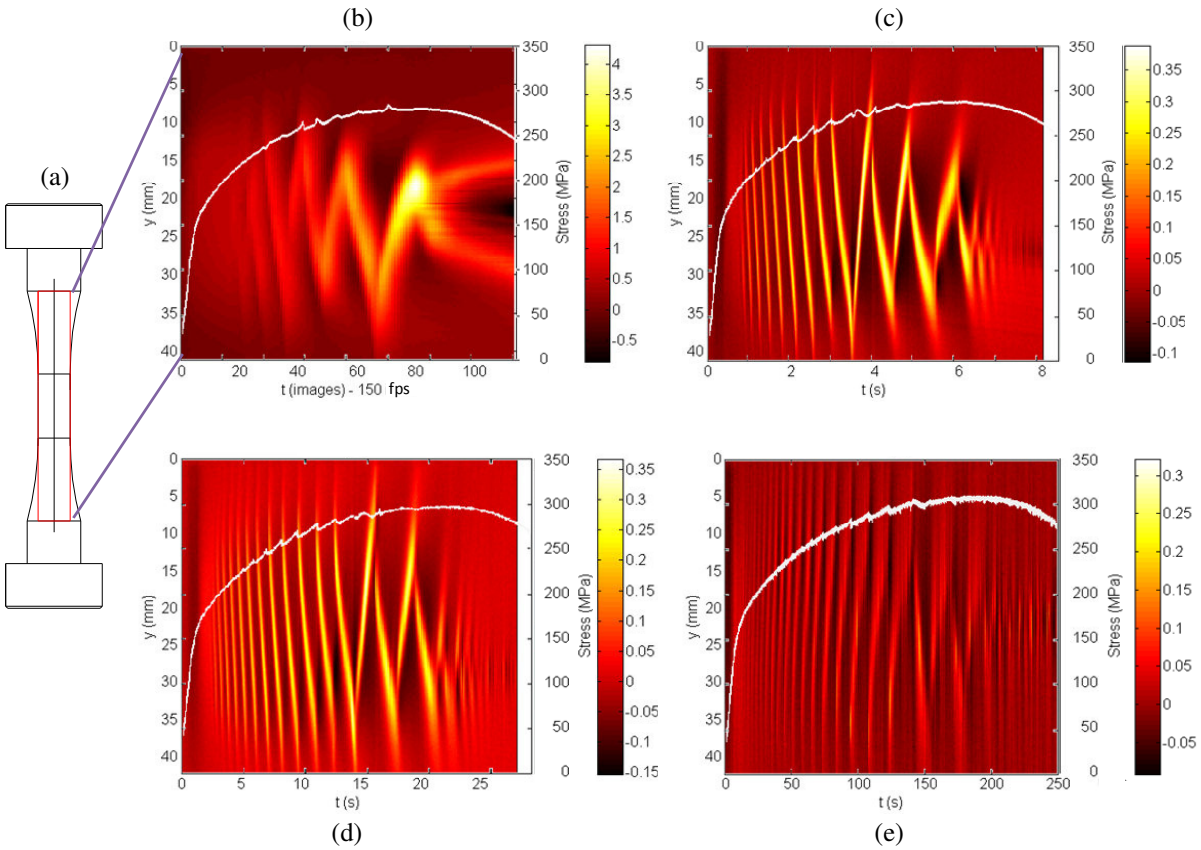

Figure 4. Temperature change ΔT given by (1) versus time as measured by thermography along the vertical center line of the specimens. For completeness, the stress-time curve is superposed. (a) Round specimen ($\phi = 6\,\text{mm}$) with the imaged zone indicated; (b) $\dot{\varepsilon} = 10^{-1}\,\text{s}^1$; (c) $\dot{\varepsilon} = 10^{-2}\,\text{s}^1$; (d) $\dot{\varepsilon} = 2.8 \times 10^{-3}\,\text{s}^1$; (e) $\dot{\varepsilon} = 3.33 \times 10^{-4}\,\text{s}^{-1}$.

ranging from 1 mm to 9 mm. For the same tests, Figure 7 displays the orientations of the observed bands as a function of the nominal strain. This orientation is measured by the inclination of the band with respect to the tension axis. While this orientation seems to be well defined around 60° for small thicknesses, it varies somewhat between 60° and 90° when this thickness is increased.

3.2. ***Portevin–Le Châtelier effect on notched specimens.*** Seven tests, called T1, T2, T3,T4, T5, T6, and T7 in the sequel, were carried out on the flat U-notched and V-notched specimen geometries described in Section 2 (see Table 1) in order to determine the effects of the specimen geometry on the characteristics of the deformation bands and their propagation. All tests were carried out in displacement control with a fixed clamp velocity. Table 1 presents a brief summary of the tests.

Before moving to a detailed analysis of the PLC deformation bands on notched specimens, let us first compare the morphology of these bands for all types of specimens used in this investigation. Figure 8 shows the imaged zones in thermography for all the studied specimens, as well as the associated morphology of the observed deformation bands at given instants of the loading process.

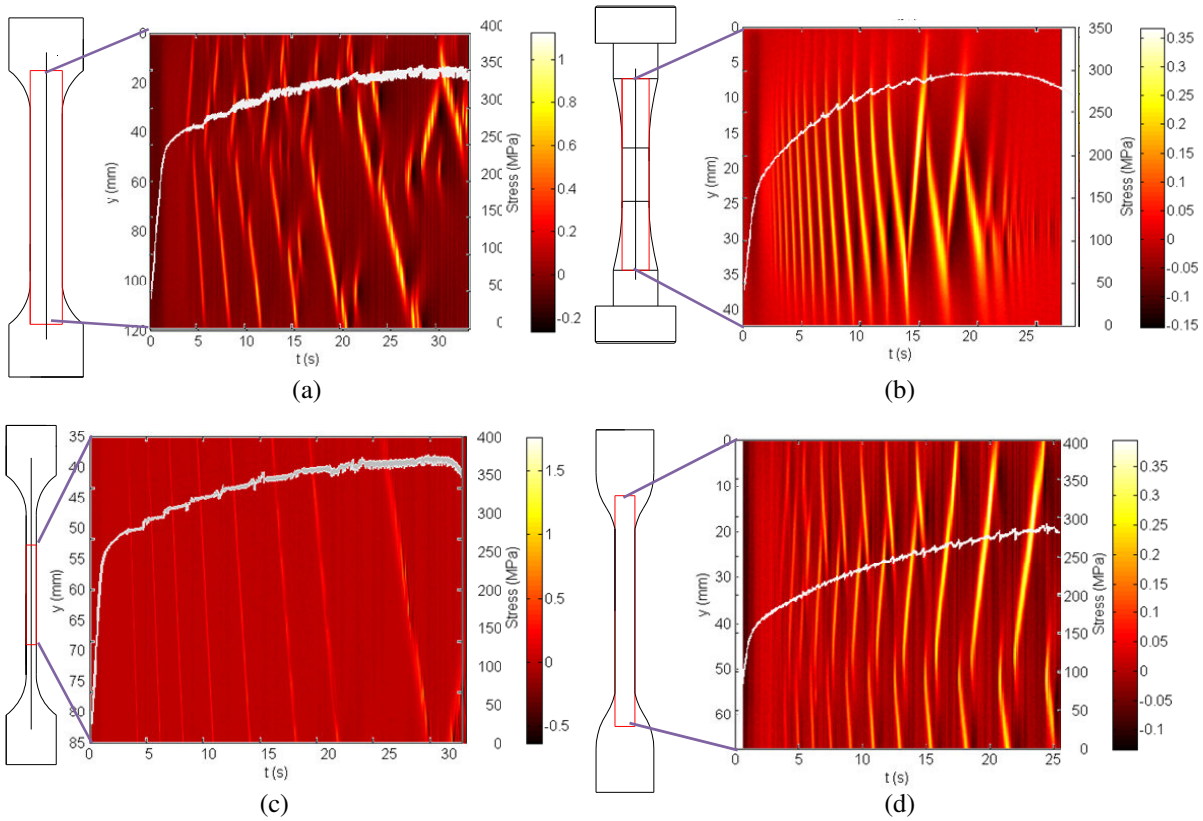

Figure 5. Temperature change ΔT given by (1) versus time as measured by thermography along the vertical center line for tension tests on different specimens at the same strain-rate of $2.8 \times 10^{-3}\,\mathrm{s}^{-1}$. For completeness, the stress-time curve is also superposed. (a) Smooth flat specimen ($15 \times 2\,\mathrm{mm}^2$); (b) round specimen ($\phi = 6\,\mathrm{mm}$); (c) smooth flat specimen ($4 \times 4\,\mathrm{mm}^2$); (d) smooth flat specimen ($6 \times 5\,\mathrm{mm}^2$).

Figures 9a and 9b show the force-displacement response for tests T1, T2, T3, and T4 up to failure. Figures 9c and 9d are zooms of the ends of these tests, showing more clearly the serrations observed

Test	Cross head velocity ($\mathrm{mm\,s}^{-1}$)	Notch
T1	0.955	U-notched specimen – $R = 0.4$
T2	0.955	U-notched specimen – $R = 0.8$
T3	0.955	U-notched specimen – $R = 2.0$
T4	0.955	Cracked specimen – (One 0° V-notch)
T5	0.0975	V-notched specimen – 30°
T6	0.0975	V-notched specimen – 45°
T7	0.0975	V-notched specimen – 60°

Table 1. Summary of all the tests carried out in the present study.

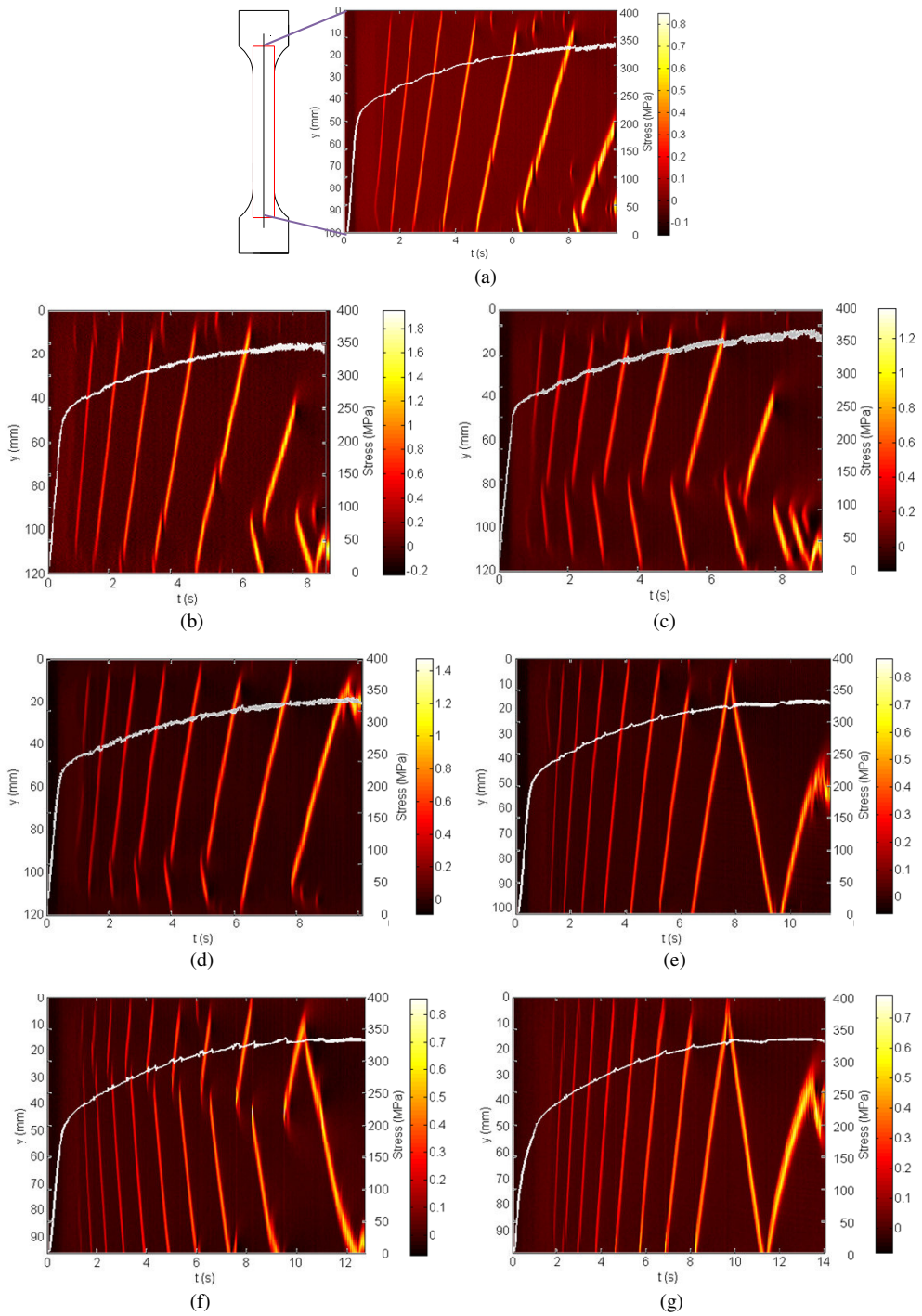

Figure 6. Temperature change versus time as measured by thermography along vertical center line of specimens, with stress-time curve superposed. Nominal strain rate is $10^{-2}\,\mathrm{s}^{-1}$ and geometry is a smooth flat specimen with 15 mm width. The thickness e is (a) 1 mm, (b) 2 mm, (c) 3 mm, (d) 4 mm, (e) 5 mm, (f) 7 mm, and (g) 9 mm.

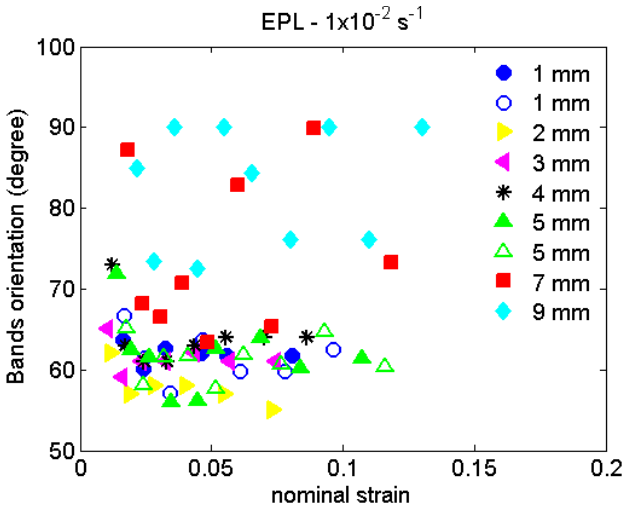

Figure 7. Band orientation versus nominal strain obtained during tension tests on different smooth flat specimens with the same 15 mm width but different thicknesses (1, 2, 3, 4, 5, 7, and 9 mm), at a nominal strain-rate of $10^{-2}\,\mathrm{s}^{-1}$.

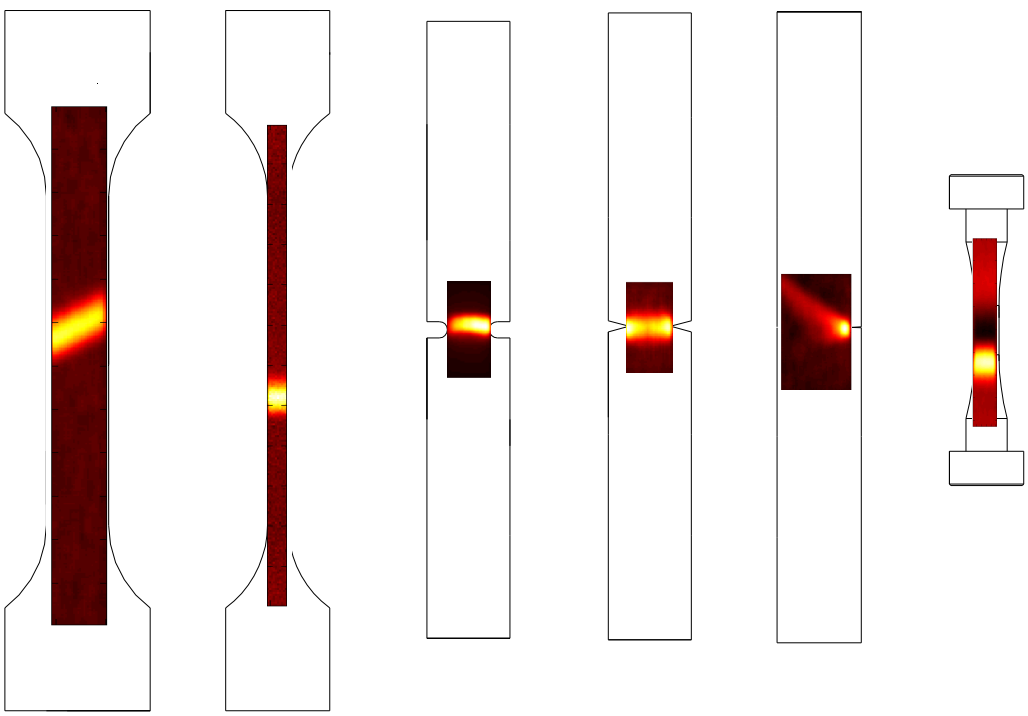

Figure 8. Two-dimensional view of PLC bands for different specimen geometries measured by thermography during tensile tests: (a) flat specimen, (b) prismatic specimen, (c) U-notched specimen, (d) V-notched specimen, (e) cracked specimen, and (f) round specimen. The temperature change ΔT given by (1) is displayed here.

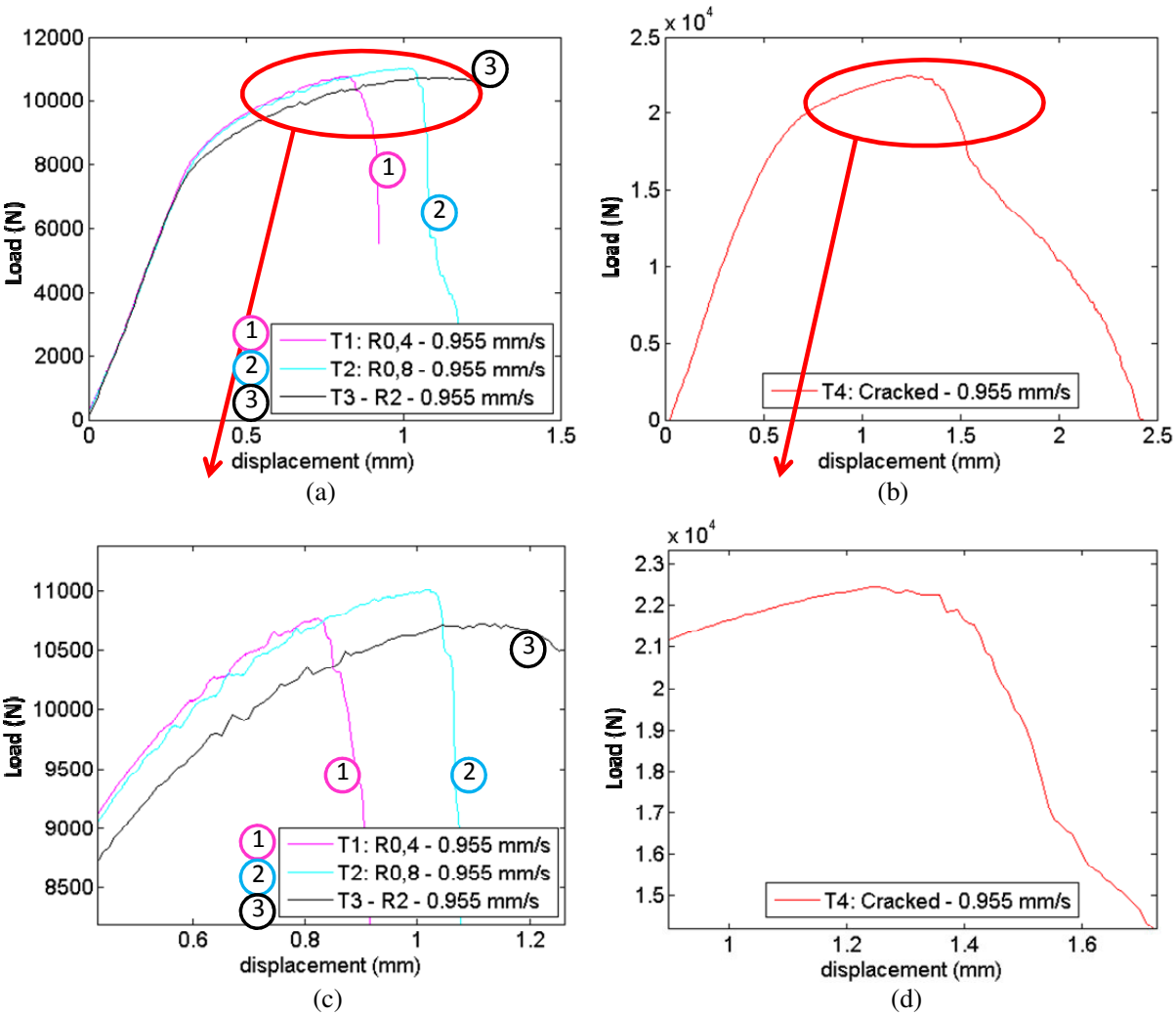

Figure 9. Force versus displacement for all tests: (a) T1, T2, and T3; (b) T4; (c) zoom of (a); (d) zoom of (b).

during the tests, signaling the presence of the deformation bands. These serrations only occur after a certain time of plastic strain. The observed final failure mode is a shear failure through the thickness of the specimen. As an illustration, the broken specimen from T3 is shown in Figure 10.

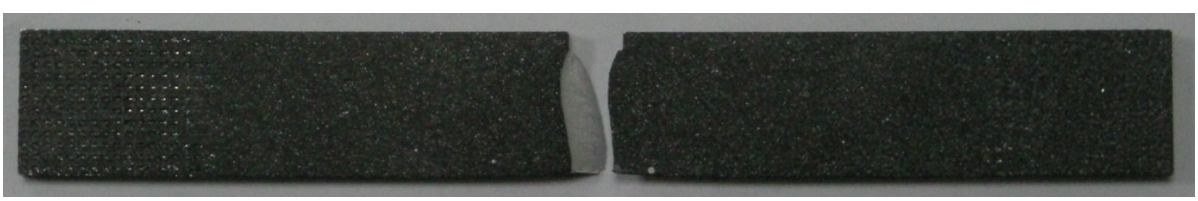

Figure 10. Broken specimen from all tests illustrating the observed shear modes for T3.

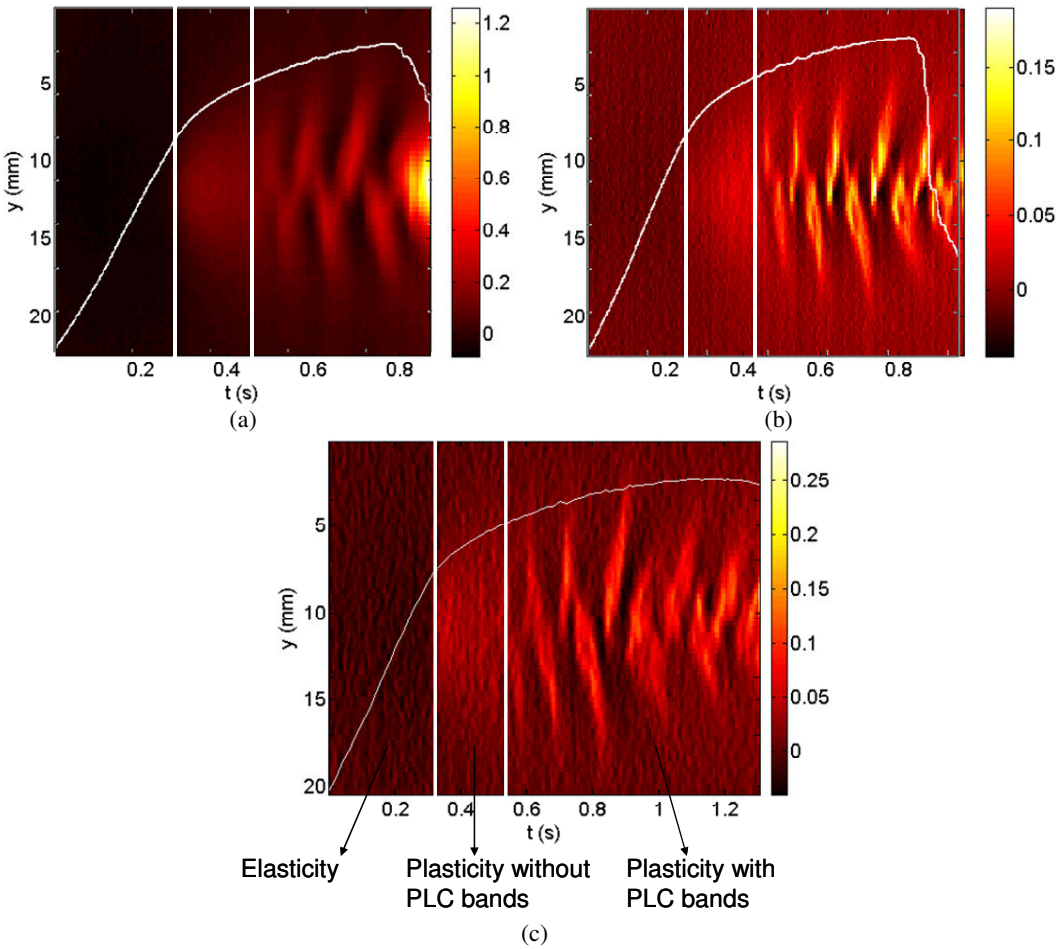

Figure 11. Temperature change $\Delta T(4.84, y, t)$ measured along the vertical line $x = 4.84$, in comparison with the response force-time of the test. Note clearly the elasticity, the plasticity without PLC bands, and the plasticity with PLC bands for the three tests: (a) T1, (b) T2, and (c) T3.

Figure 11 shows a summary of tests T1, T2, and T3 carried out at average strain rates of $7.16 \times 10^{-1}\,\mathrm{s}^{-1}$, $7.16 \times 10^{-2}\,\mathrm{s}^{-1}$, and $7.16 \times 10^{-3}\,\mathrm{s}^{-1}$, respectively, and displays the load-time response (thin white line) superposed on the time evolution of the temperature change observed in the specimen along the vertical line (and longitudinal axis of the specimen) $x = 4.84\,\mathrm{mm}$.

The thermal information of Figure 11 clearly shows three regions separated by thick vertical lines and representing respectively the elastic response of the specimen (the rather dark area), the plastic response prior to the development of the PLC (where the temperature slightly increases due to plastic dissipation), and finally the plastic response with the PLC and associated deformations bands. In this last area, one can observe, through the spatiotemporal distribution of temperature changes along the vertical axis of the specimen, the nucleation and propagation of the deformation bands. Similar responses are observed in the three tests T1, T2, and T3.

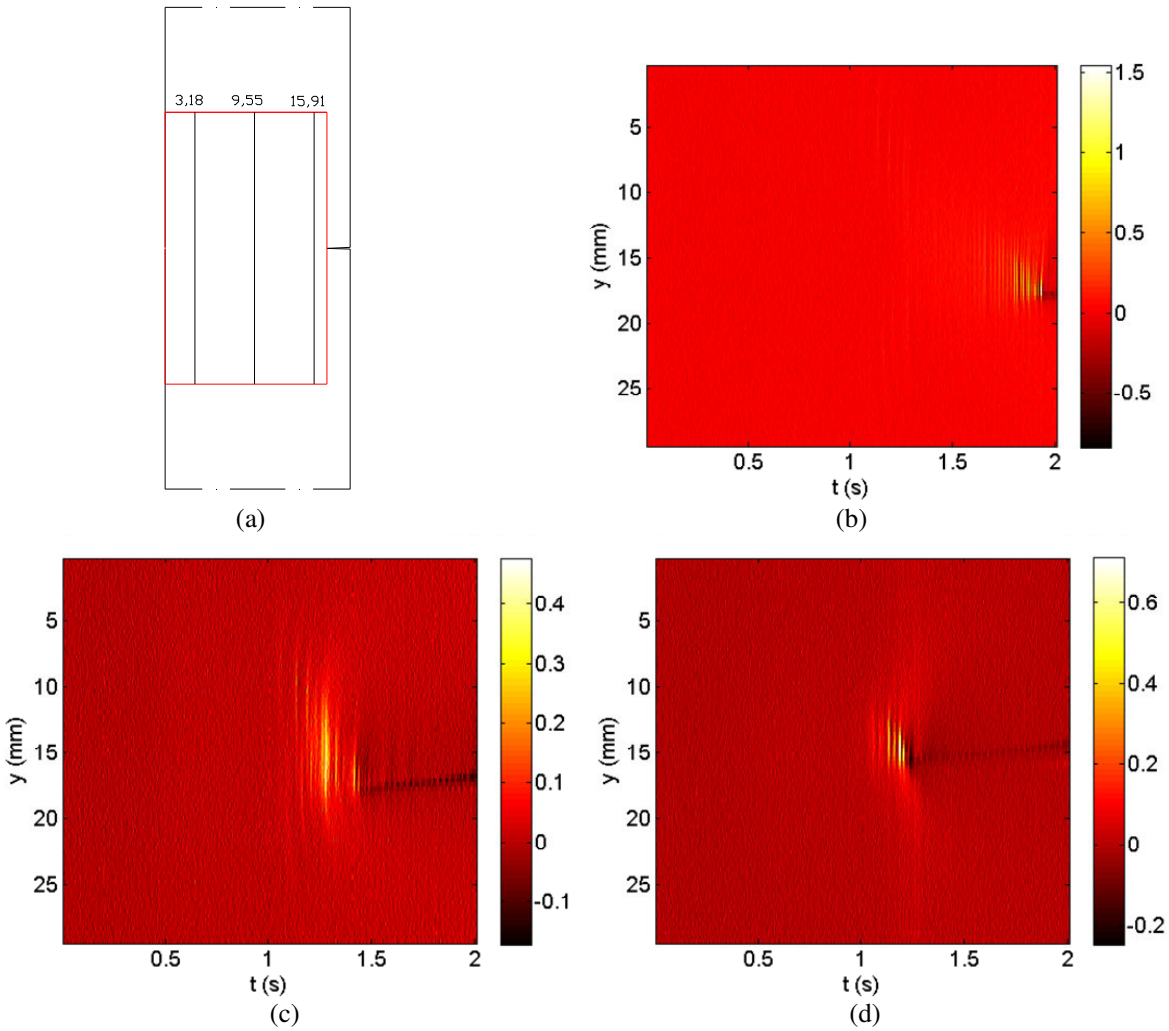

Figure 12. (a) Cracked specimen with the imaged area indicating the three vertical lines used for presenting the experimental results; (b) temperature change $\Delta T(x, y, t)$ measured along the vertical line $x = 3.18$; (c) temperature change $\Delta T(x, y, t)$ measured along the vertical line $x = 9.55$; (d) temperature change $\Delta T(x, y, t)$ measured along the vertical line $x = 15.91$.

In the case of the cracked specimen (T4), we present in Figure 12 the history of the temperature change $\Delta T(x, y, t)$ versus time at three different locations on the specimen, namely $x = 3.18$, $x = 9.55$, and $x = 15.91$ (close to the initial crack tip), as depicted in Figure 12a. One observes that there are PLC bands and these bands are stuck in the crack tip. In Figure 12b ($x = 3.18$), to where the crack has propagated, it is only at the end of the test that we could see the traces of deformation bands on the spatiotemporal analysis, when the crack tip has approached this position. In Figures 12c and 12d we observe the progress of the crack, and one can see a similar situation as in Figure 12b. One can also observe that bands do not propagate along the specimen, but are trapped at the crack tip.

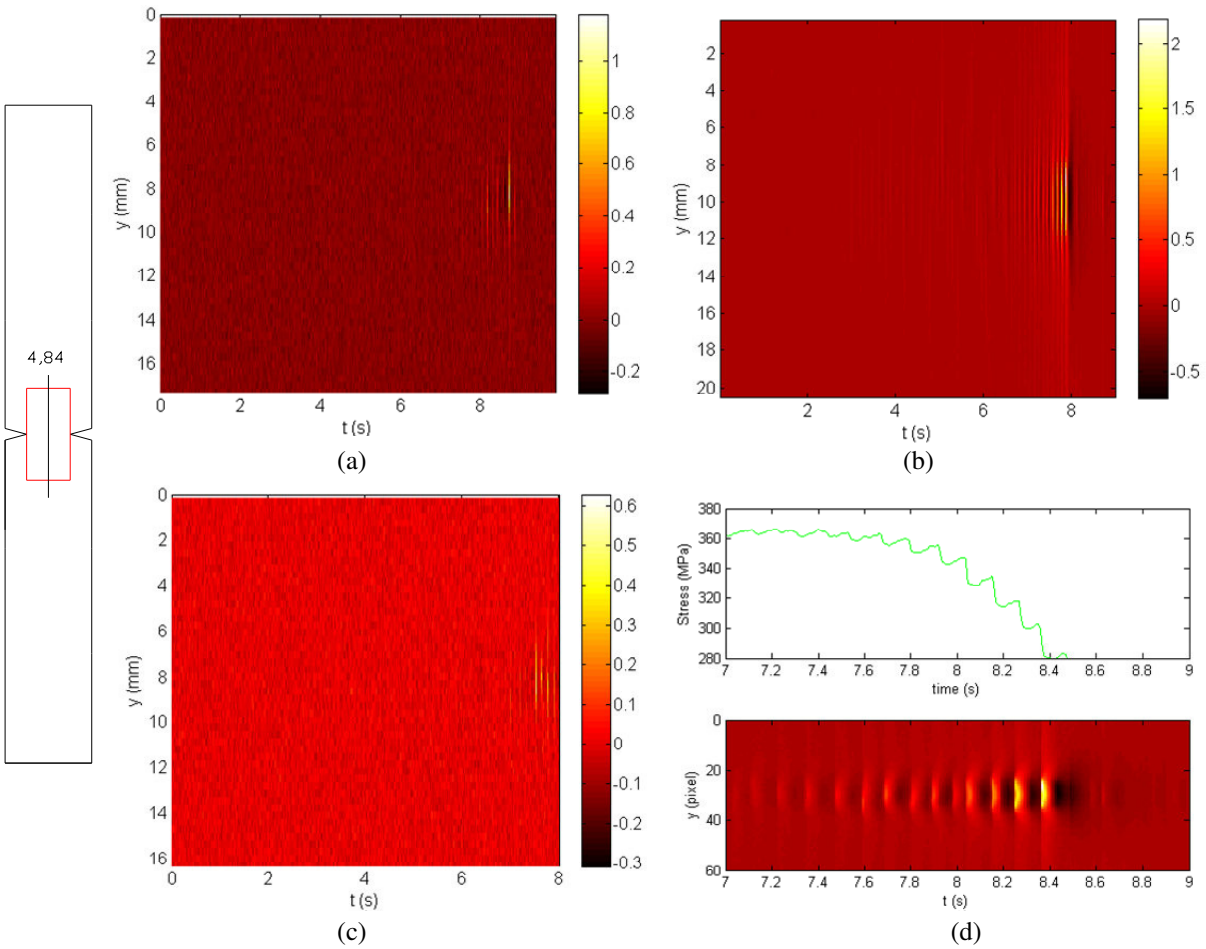

Figure 13. Temperature change $\Delta T(x, y, t)$ measured along the vertical line $x = 4.84$ for the V-notched specimens: (a) T5 (30°), (b) T6 (45°), (c) T7 (60°), and (d) T6 (V45°), showing its comparison with the response force-time at the end of the test.

Similar representations are provided in Figure 13 for the V-notched specimens.

Figures 14a, 14b, and 14c compare, for the three tests T1, T2, and T3 on U-notched specimens, the incremental strain maps (on the left sides) obtained by DIC and the temperature change $\Delta T(x, y, t)$ (on the right sides) at different time locations. As seen, the agreement is very good.

At these time locations, a deformation band is seen above or below the minimal section of the specimen. The movement of the band is actually a bowing around and above this minimal section followed by a bowing around and below the minimal section. This is better seen in Figure 11, where in the beginning of the PLC phenomenon a deformation band nucleates in the minimal section of the specimen and bows down until it disappears, after which another band develops, still in the minimal section, and bows up this time until it disappears again. The whole process is repeated again until failure of the specimens in Figure 11 for the three tests.

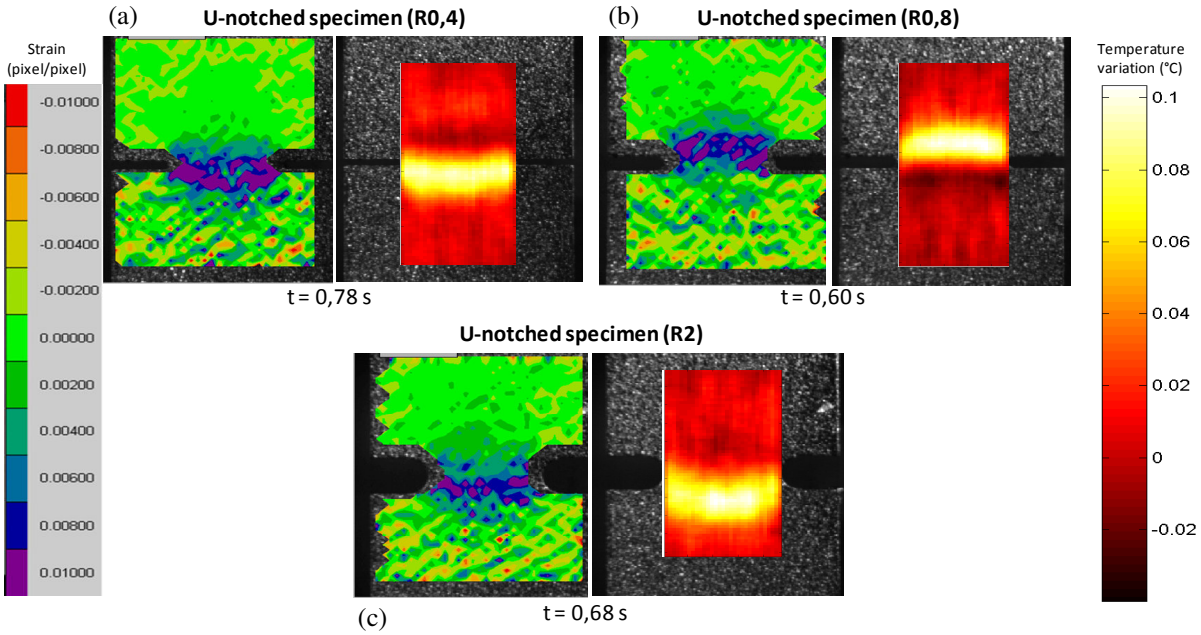

Figure 14. Longitudinal strain and temperature change ΔT maps as obtained from DIC and DIT on the two opposite sides of each specimen for tests on notched specimens: (a) T1, (b) T2, and (c) T3.

To give more emphasis to the behavior of the bands, we choose T3 and give more details on the movements of the deformation bands. Figure 15 compares the temperature changes observed in the width of the specimen. To that purpose, it displays for the whole test (except for the final part, which includes the fracture of the specimen) the temperature changes $\Delta T(x, y, t)$ along the vertical lines $x = 0.65$, $x = 4.84$, and $x = 9.68$ of the specimen for the imaged area, shown in Figure 1c. Different levels of temperature are reached from the left to the right of the specimen (with the smallest on the left).

Figures 16 and 17 show the temperature and axial strain (ε_{yy}) histories during the whole test at the same locations mentioned above, the middle and the bottom of the imaged zone shown in Figure 1b. Both strain and temperature histories display the classical staircase behavior characteristic of the PLC

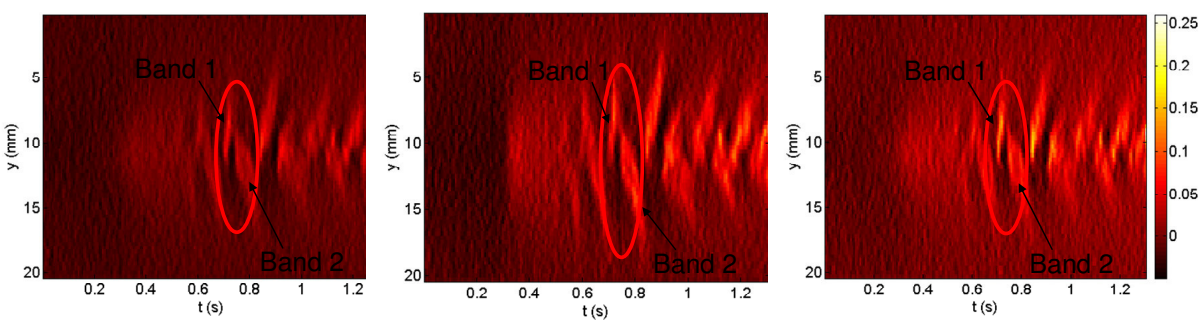

Figure 15. Temperature change measured along the vertical lines $x = 0.65$ (left), $x = 4.84$ (center), and $x = 9.68$ (right) for T3.

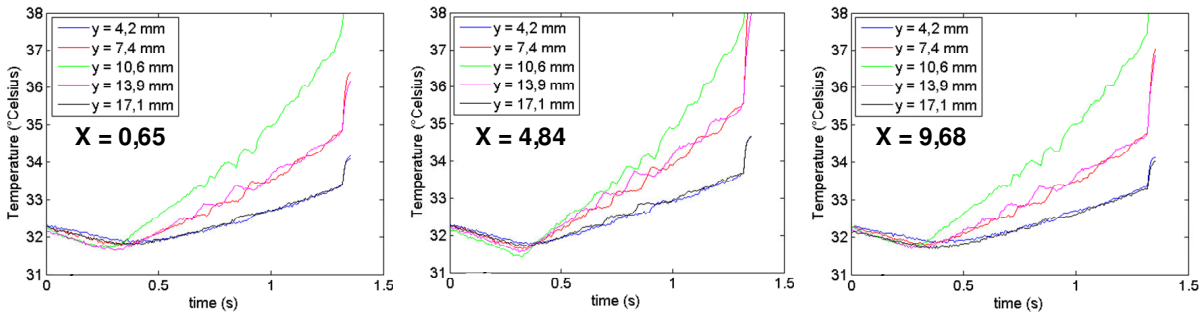

Figure 16. Temperature histories for T3 at the different locations indicated in Figure 1b.

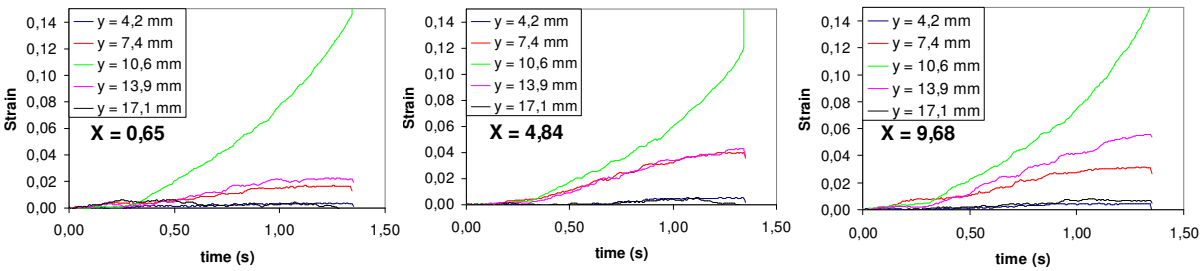

Figure 17. Longitudinal strain histories for T3 at the different locations indicated in Figure 1b.

effect, where each stair is the manifestation of a band passing at these locations. Figure 16 shows clearly a higher temperature increase in the minimal section of the specimen ($y = 10.6$ mm), where the stress concentration is higher. Figure 17 shows that the strain is higher near the notch at the minimal section.

Figures 18 and 19 show the temperature along the three vertical lines ($x = 0.65$, $x = 4.84$, and $x = 9.68$) at different time instants. Beside the global rise in temperature due to plasticity, one can also see the propagation of the deformation bands (see the location of the maximum temperature that moves to the left in Figure 18 and to the right in Figure 19). Figure 18 shows a band that propagates from the minimal section (the dashed line) to the top side of the specimen. Figure 19 show another one that propagates

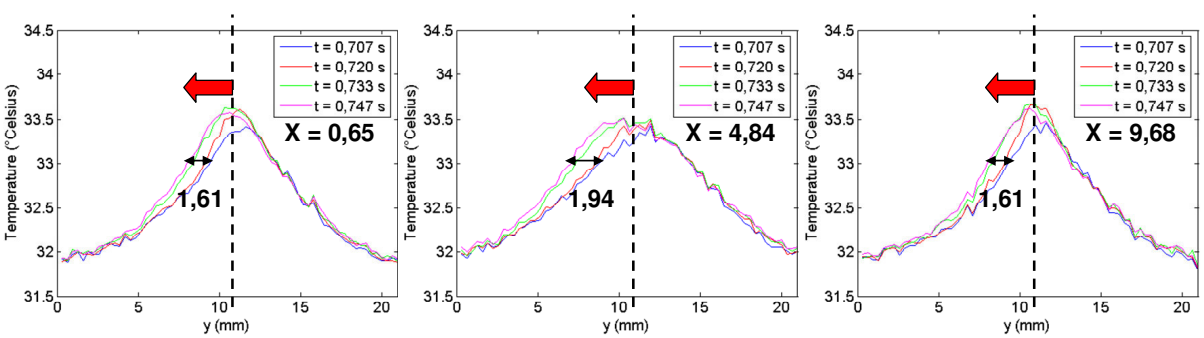

Figure 18. Propagation of band 1 shown in Figure 15. The traveling distance of the band is higher in the minimal section ($x = 4.84$) than at the roots of the notches ($x = 0.65$ and $x = 9.68$) leading to the slightly curved morphology of the band.

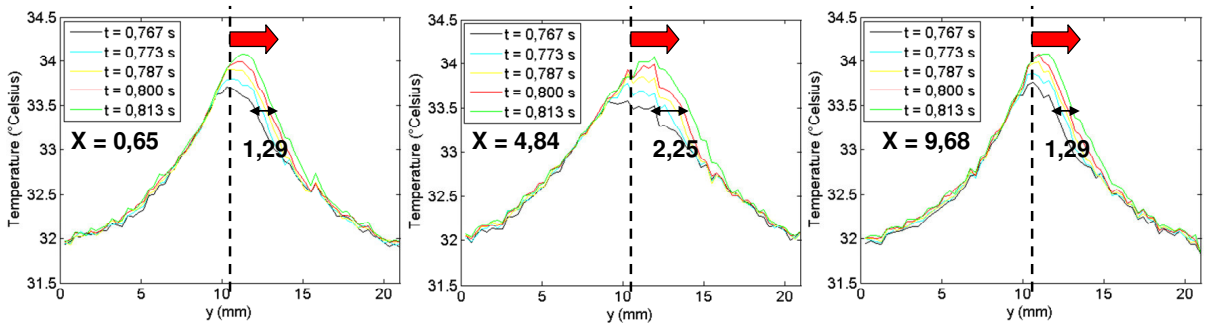

Figure 19. Propagation of band 2 shown in Figure 15. The travel distance of the band is higher in the minimal section ($x = 4.84$) than at the roots of the notches ($x = 0.65$ and $x = 9.68$) leading to the slightly curved morphology of the band.

from the minimal section to the bottom side, as one can also see in Figures 11 and 15. One can also observe the differences in the band propagation, between the centerline of the specimen ($x = 10.6$) and near the roots ($x = 0.65$ and $x = 9.68$) leading to the bowing of the band around the minimal section.

Figures 20 and 21 give the same results as Figures 18 and 19 but display rather the temperature changes $\Delta T(x, y, t)$ of relation (1) instead of the temperature. This is more representative of the PLC effect and

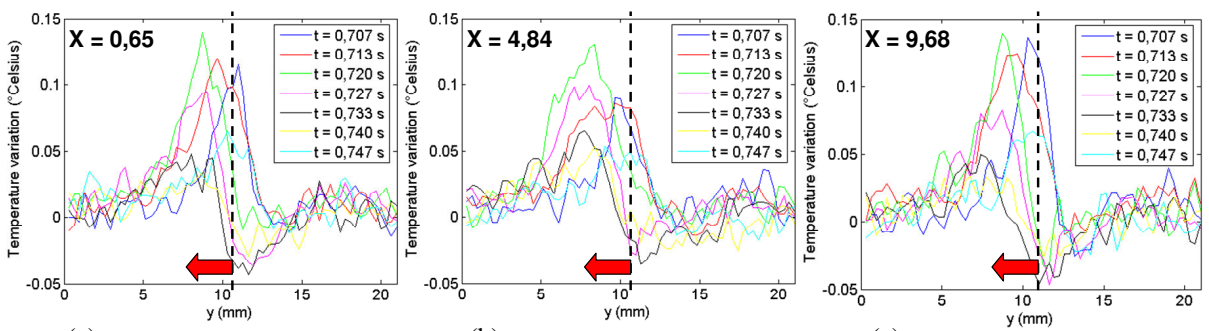

Figure 20. Temperature increments ΔT profile showing the propagation of band 1 of Figure 15.

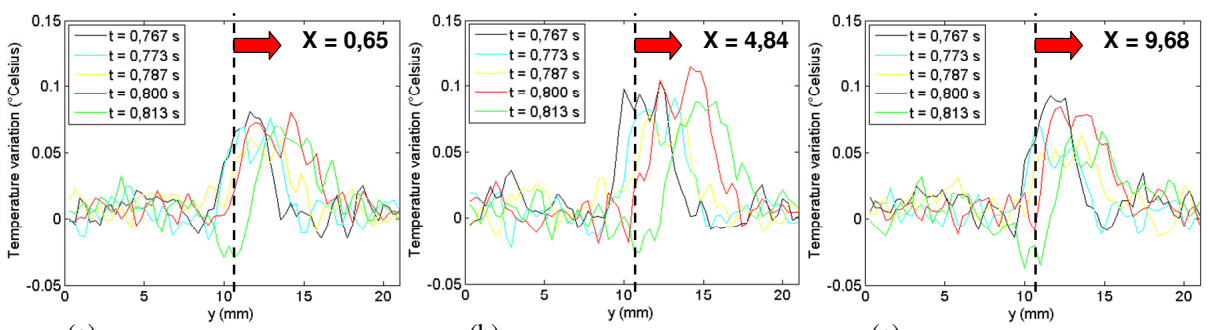

Figure 21. Profiles of temperature increments ΔT associated with the propagation of band 2 shown in Figure 15.

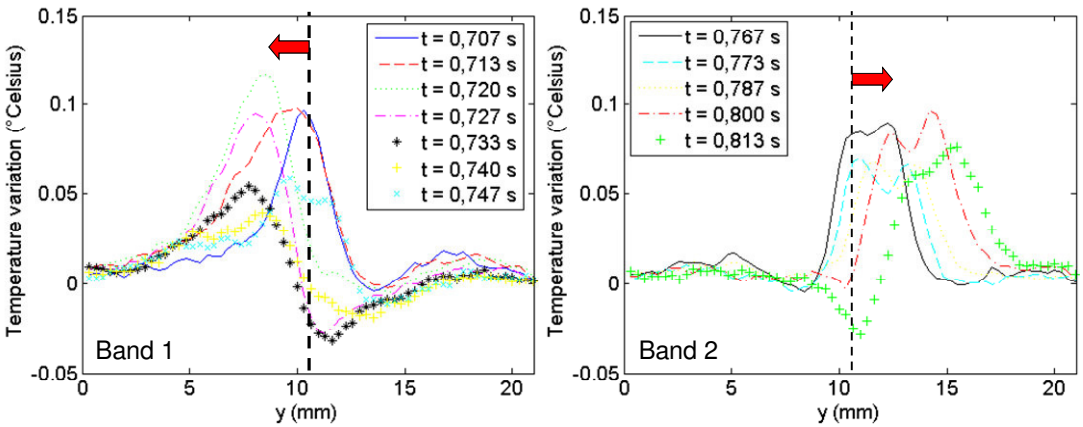

Figure 22. Temperature variation as a function of y, showing the same bands, 1 and 2: average of temperature variations of Figures 20a, 20b, and 20c (left); and average of temperature variations of Figures 21a, 21b, and 21c (right).

is plotted at different times along the lines $x = 0.65$, $x = 4.84$, and $x = 9.68$. While visible in these figures, the growth (temperature increase), propagation, and decay (temperature decrease) of the bands are better seen in Figure 22, obtained by a filtering of Figures 20 and 21. This filtering is simply carried out by taking the average of the temperature distributions at $x = 0.65$, $x = 4.84$, and $x = 9.68$. Indeed, on the left of Figure 22, one can clearly distinguish the growth of a band between times $t = 0.707$ s and $t = 0.720$ s, and then its decay from $t = 0.720$ s to $t = 0.740$ s. During this period, the band moved to the left, then slightly returned at the end. Just after this, another band is seen growing ($t = 0.747$ s) and continues its growth and decay on the right side of Figure 22 (from $t = 0.767$ s to $t = 0.800$ s), but now to the right.

4. Conclusions

Digital infrared thermography and digital image correlation are important tools for observing and evaluating the nucleation, growth, decay, and morphology of Portevin–Le Châtelier deformation bands (as well as other localized and propagating instabilities) under general loading conditions. Application of these tools to various specimens indeed allows exhibiting the main features of the development and propagation of these bands, which, for the cross-head velocity considered here, are seen to be trapped in the vicinity of the minimal cross section and bow up and down around this section for U-notched specimens. In the case of the cracked specimen, bands are stuck at the crack tip. This information is important in modeling dynamic strain aging phenomena and in discriminating between the various proposals existing in the literature. This is currently under investigation.

References

[Benallal et al. 2008a] A. Benallal, T. Berstad, T. Børvik, O. S. Hopperstad, and R. Nogueira de Codes, "Effects of strain rate on the characteristics of PLC deformation bands for AA5083-H116 aluminium alloy", *Philos. Mag.* **88**:28–29 (2008), 3311–3338.

[Benallal et al. 2008b] A. Benallal, T. Berstad, T. Børvik, O. S. Hopperstad, I. Koutiri, and R. Nogueira de Codes, "An experimental and numerical investigation of the behaviour of AA5083 aluminium alloy in presence of the Portevin–Le Chatelier effect", *Int. J. Plast.* **24**:10 (2008), 1916–1945.

[van den Beukel 1980] A. van den Beukel, "On the mechanism of serrated yielding and dynamic strain ageing", *Acta Metall.* **28**:7 (1980), 965–969.

[Clausen et al. 2004] A. H. Clausen, T. Børvik, O. S. Hopperstad, and A. Benallal, "Flow and fracture characteristics of aluminium alloy AA5083-H116 as function of strain rate, temperature and triaxiality", *Mater. Sci. Eng. A* **364**:1–2 (2004), 260–272.

[Cottrell 1953a] A. H. Cottrell, *Dislocations and plastic flow in crystals*, University Press, Oxford, 1953.

[Cottrell 1953b] A. H. Cottrell, "A note on the Portevin–Le Chatelier effect", *Philos. Mag.* (7) **44**:355 (1953), 829–832.

[Curtin et al. 2006] W. A. Curtin, D. L. Olmsted, and L. G. Hector, Jr., "A predictive mechanism for dynamic strain ageing in aluminium-magnesium alloys", *Nat. Mater.* **5**:11 (2006), 875–880.

[Hild and Roux 2006] F. Hild and S. Roux, "Digital image correlation: from displacement measurement to identification of elastic properties – a review", *Strain* **42**:2 (2006), 69–80.

[Hopperstad et al. 2007] O. S. Hopperstad, T. Børvik, T. Berstad, O.-G. Lademo, and A. Benallal, "A numerical study on the influence of the Portevin–Le Chatelier effect on necking in an aluminium alloy", *Model. Simul. Mater. Sci. Eng.* **15**:7 (2007), 747–772.

[Kubin and Estrin 1985] L. P. Kubin and Y. Estrin, "Portevin–Le Chatelier effect in deformation with constant stress rate", *Acta Metall.* **33**:3 (1985), 397–407.

[McCormick 1988] P. G. McCormick, "Theory of flow localisation due to dynamic strain ageing", *Acta Metall.* **36**:12 (1988), 3061–3067.

[Mulford and Kocks 1979] R. A. Mulford and U. F. Kocks, "New observations on the mechanisms of dynamic strain aging and of jerky flow", *Acta Metall.* **27**:7 (1979), 1125–1134.

[Nabarro 1948] F. R. N. Nabarro, *Report on strength of solids*, pp. 38, Physical Society, London, 1948.

[Neuhäuser et al. 2004] H. Neuhäuser, F. B. Klose, F. Hagemann, J. Weidenmüller, H. Dierke, and P. Hähner, "On the PLC effect in strain-rate and stress-rate controlled tests: studies by laser scanning extensometry", *J. Alloy. Compd.* **378**:1–2 (2004), 13–18.

[Picu 2004] R. C. Picu, "A mechanism for the negative strain-rate sensitivity of dilute solid solutions", *Acta Mater.* **52**:12 (2004), 3447–3458.

[Rizzi and Hähner 2004] E. Rizzi and P. Hähner, "On the Portevin–Le Chatelier effect: theoretical modeling and numerical results", *Int. J. Plast.* **20**:1 (2004), 121–165.

[Robinson and Shaw 1994] J. M. Robinson and M. P. Shaw, "Observations on deformation characteristics and microstructure in an Al-Mg alloy during serrated flow", *Mater. Sci. Eng. A* **174**:1 (1994), 1–7.

[Sleeswyk 1958] A. W. Sleeswyk, "Slow strain-hardening of ingot iron", *Acta Metall.* **6**:9 (1958), 598–603.

Received 7 Aug 2010. Revised 30 Nov 2010. Accepted 26 Dec 2010.

RODRIGO NOGUEIRA DE CODES: nogueira@lmt.ens-cachan.fr
LMT-Cachan, ENS Cachan/CNRS/UPMC/PRES UniverSud Paris, 61 Avenue du Président Wilson, 94235 Cachan, France

AHMED BENALLAL: benallal@lmt.ens-cachan.fr
LMT-Cachan, ENS Cachan/CNRS/UPMC/PRES UniverSud Paris, 61 Avenue du Président Wilson, 94235 Cachan, France

JOURNAL OF MECHANICS OF MATERIALS AND STRUCTURES

jomms.org

Founded by Charles R. Steele and Marie-Louise Steele

See http://jomms.org for submission guidelines.

JoMMS (ISSN 1559-3959) is published in 10 issues a year. The subscription price for 2011 is US $520/year for the electronic version, and $690/year (+$60 shipping outside the US) for print and electronic. Subscriptions, requests for back issues, and changes of address should be sent to Mathematical Sciences Publishers, Department of Mathematics, University of California, Berkeley, CA 94720–3840.

JoMMS peer-review and production is managed by EditFLOW® from Mathematical Sciences Publishers.

PUBLISHED BY

mathematical sciences publishers

http://msp.org/

A NON-PROFIT CORPORATION

Typeset in LaTeX

Journal of Mechanics of Materials and Structures

Volume 6, No. 7-8 September–October 2011

Special issue

Eleventh Pan-American Congress of Applied Mechanics (PACAM XI)

Preface — Adair R. Aguiar — 949

Influence of specimen geometry on the Portevin–Le Châtelier effect due to dynamic strain aging for the AA5083-H116 aluminum alloy — Rodrigo Nogueira de Codes and Ahmed Benallal — 951

Dispersion relations for SH waves on a magnetoelectroelastic heterostructure with imperfect interfaces — J. A. Otero, H. Calas, R. Rodríguez, J. Bravo, A. R. Aguiar and G. Monsivais — 969

Numerical linear stability analysis of a thermocapillary-driven liquid bridge with magnetic stabilization — Yue Huang and Brent C. Houchens — 995

Numerical investigation of director orientation and flow of nematic liquid crystals in a planar 1:4 expansion — Pedro A. Cruz, Murilo F. Tomé, Iain W. Stewart and Sean McKee — 1017

Critical threshold and underlying dynamical phenomena in pedestrian-induced lateral vibrations of footbridges — Stefano Lenci and Laura Marcheggiani — 1031

Free vibration of a simulation CANDU nuclear fuel bundle structure inside a tube — Xuan Zhang and Shudong Yu — 1053

Nonlinear dynamics and sensitivity to imperfections in Augusti's model — D. Orlando, P. B. Gonçalves, G. Rega and S. Lenci — 1065

Active control of vortex-induced vibrations in offshore catenary risers: A nonlinear normal mode approach — Carlos E. N. Mazzilli and César T. Sanches — 1079

Nonlinear electromechanical fields and localized polarization switching of piezoelectric macrofiber composites — Yasuhide Shindo, Fumio Narita, Koji Sato and Tomo Takeda — 1089

Three-dimensional BEM analysis to assess delamination cracks between two transversely isotropic materials — Nicolás O. Larrosa, Jhonny E. Ortiz and Adrián P. Cisilino — 1103

Porcine dermis in uniaxial cyclic loading: Sample preparation, experimental results and modeling — A. E. Ehret, M. Hollenstein, E. Mazza and M. Itskov — 1125

Analysis of nonstationary random processes using smooth decomposition — Rubens Sampaio and Sergio Bellizzi — 1137

Perturbation stochastic finite element-based homogenization of polycrystalline materials — S. Lepage, F. V. Stump, I. H. Kim and P. H. Geubelle — 1153

A collocation approach for spatial discretization of stochastic peridynamic modeling of fracture — Georgios I. Evangelatos and Pol D. Spanos — 1171